Design and Implementation of a Six-Element Autonomous Active Aerodynamics System for Formula SAE

Duncan R. Kuchar*, Leonard J. Hamilton†, and Huan Xu‡
A. James Clark School of Engineering, University of Maryland, College Park, MD 20742, USA

This paper presents the design, fabrication, and validation of a fully autonomous active aerodynamics system for the 2025 University of Maryland internal combustion Formula SAE (FSAE) vehicle, also known as the Terps Racing TR25. The autonomous active aerodynamics system was showcased at the 2025 Michigan FSAE competition, receiving the Second Place Innovation Award. To resolve the conflict between high downforce required for cornering and low drag required for longitudinal acceleration and good fuel economy, a six-element active wing package was developed, comprising four actuated flaps on the front wing and two actuated flaps on the rear wing. The system is governed by a finite state machine algorithm that processes data from wheel speed, steering angle, throttle position, brake pressure, and inertial sensors to estimate vehicle states and execute coordinated actuation. To ensure reliability and adaptability, the system incorporates robust failure mitigation protocols and a driver interface for on-the-fly sensitivity tuning to match driver styles and track conditions. Computational fluid dynamics and track testing demonstrate a 49% reduction in drag coefficient (C_D from 1.44 to 0.73) between the high and low-drag configurations. Validated lap time simulations predict a 1.47-second and 42.4-second (2.6%) improvement in Autocross and Endurance dynamic events (based on the 2024 competition tracks), respectively, alongside a 7.2% increase in fuel efficiency, and a 0.08-second (1.9%) improvement in the Acceleration dynamic event. Additionally, the system enables a longitudinal center of pressure migration from 78% to 20% (% of total downforce on front tires), providing a foundation for active balance control through dynamic track states.

I. Nomenclature

A	=	frontal area, m^2
a_x, a_y	=	longitudinal/lateral acceleration, g
C_D	=	drag coefficient
C_L	=	lift coefficient
C_p	=	center of pressure, % of total downforce on front tires
F_{aero}	=	aerodynamic force, N
F_D	=	drag force, N
F_L	=	downforce (-Lift), N
F_y	=	lateral tire force, N
F_z	=	vertical tire load, N
P_{brake}	=	brake pressure, psi
Re	=	Reynolds number
T	=	throttle position, %
V	=	velocity, km/h
α	=	angle of attack, deg
δ	=	steering angle, deg
μ	=	tire friction coefficient
ρ	=	air density, $kg\,m^{-3}$

*Undergraduate Student, Aerospace Engineering Department and Institute for Systems Research, University of Maryland, 3179 Glenn L. Martin Hall Bldg #088 4298 Campus Drive, College Park, MD, USA. AIAA Student Member 1899897, Undergraduate Category
†Visiting Associate Professor, Mechanical Engineering Department, University of Maryland, College Park, MD, USA
‡Associate Professor, Aerospace Engineering Department and Institute for Systems Research, University of Maryland, College Park, MD, USA.



Fig. 1 Terps Racing TR25 featuring the autonomous six-element active aerodynamics package during the FSAE 2025 endurance competition at the Michigan International Speedway.

II. Introduction

Racing vehicle aerodynamic design pursues three primary objectives. The first is the reduction of aerodynamic drag, which directly correlates to improved energy efficiency and increased top speeds. The second is the production of negative lift, or "downforce." In a racing context, downforce is critical because it increases the vertical load (F_z) on the tires without the penalty of added mass inertia. Because the lateral force capability of a tire (F_y) is a function of the vertical load and the friction coefficient (μ), increasing F_z directly increases the available grip for cornering [1]. The third goal is the improvement of vehicle controllability and driver comfort. In motorsport, this translates to aerodynamic stability, especially ensuring the Center of Pressure (C_p) remains predictable (typically slightly behind the center of gravity) to give the driver confidence at the F_y limit of the tires. If the C_p is in front of the vehicle's center of mass, drivers may experience oversteer at high speeds (as the forces on the vehicle become dominated by aerodynamic loads). Likewise, if the C_p is behind the vehicle's center of mass, drivers may experience understeer.

The magnitude of these aerodynamic forces is governed by the dynamic pressure equation [2], shown in Eq. (1), where the constant C can be C_L or C_D for lift and drag respectively.

$$F_{aero} = \frac{1}{2}\rho V^2 C A \tag{1}$$

At 80 km/h, the TR25 generates nearly enough downforce to double its effective F_z, showing the significant impact of aerodynamics in motorsport. Notably, because aerodynamic forces scale quadratically with velocity, the penalty for inefficient aerodynamics, or a poorly placed C_p becomes severe at high speeds.

This creates a fundamental conflict in racecar design: high downforce is required for cornering grip, but the induced drag associated with high-lift wings penalizes straight-line acceleration and fuel efficiency. In the Formula SAE (FSAE) collegiate design competition, this trade-off is particularly acute. FSAE dynamic events include a 75-meter straight-line acceleration (potential 100 points), 800-meter autocross (potential 125 points), 22km endurance (including fuel efficiency scoring, potential 375 points), and a figure-eight skidpad to test maximum F_y (potential 75 points). Both autocross and endurance are characterized by low-speed, transient cornering sequences that reward aggressive high-lift devices, interspersed with acceleration zones where drag becomes a significant factor.

The design space for addressing this conflict is tightly constrained by the FSAE Rules [3]. Aerodynamic devices must be contained within specific geometric limits. Furthermore, the rules explicitly prohibit powered ground effects and mandate that all aerodynamic devices remain rigid, with minimal aeroelasticity or flutter allowed under load. Whereas static multi-element wing packages have become ubiquitous in the series to address cornering requirements, they inherently limit straight-line performance.

To decouple these conflicting requirements, active aerodynamic systems have emerged as a critical area of development. In Formula 1, the Drag Reduction System (DRS) allows for rear wing adjustment to facilitate overtaking, and the upcoming 2026 technical regulations will expand this to include active front wings, mirroring the six-element configuration developed in this work. Within the collegiate sphere, prior research demonstrated the feasibility of active wings for FSAE applications [4]. However, most existing implementations rely on driver actuation and do not have continuous airfoil control.

Unlike conventional driver-actuated systems (such as F1 DRS), the TR25 architecture employs a novel Finite State Machine (FSM) algorithm. By fusing data from seven onboard sensors, the system autonomously identifies the vehicle's dynamic state and actuates a four-active-element front wing and two-active-element rear wing accordingly.

This approach achieves a 49% reduction in drag during acceleration while maintaining maximum downforce during cornering, effectively optimizing the V^2 relationship for both straight-line speed and cornering grip.

The active aerodynamics package is a complex mechatronic system comprising three distinct sub-domains: mechanical actuation, electronic hardware, and control software, described in the next three sections. Figure 2 illustrates the high-level architecture and data flow, detailing how sensor inputs are processed to result in physical wing actuation.

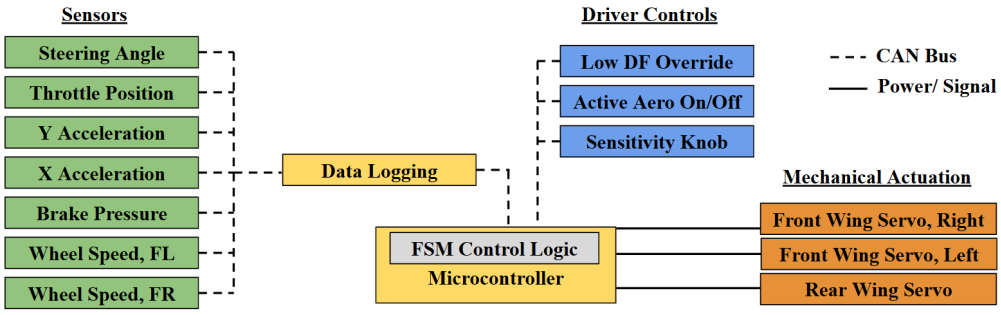


Fig. 2 System architecture diagram illustrating the data flow from onboard sensors, through the Controller Area Network (CAN) bus and FSM, to the mechanical servo actuation, changing the airfoil positions.

The data logging systems used were a Performance Electronics 3 (PE3) engine control unit and a RaceCapture MkIV data logger. The microcontroller was a Feather RP2040 Controller Area Network (CAN) selected for its CAN bus interface, microcontroller outputs, and processing speed. Servos, sensors, driver controls, and data will be discussed more in Section IV.

III. Aerodynamic and Mechanical Design

The development of the active aerodynamics package required a tightly coupled approach between aerodynamic optimization and mechanical feasibility. The design process progressed from two-dimensional airfoil selection to three-dimensional full-vehicle simulation (including ride height sweeps, velocity sweeps, and cornering simulations) followed by the mechanical design of the actuation kinematics and structural validation.

A. Computational Fluid Dynamics (CFD) Methodology

To ensure the accuracy of the aerodynamic predictions, a rigorous CFD methodology was established using Siemens STAR-CCM+. The simulation framework utilized a Reynolds-Averaged Navier-Stokes (RANS) solver with the $k-\omega$ SST-Menter turbulence model, chosen for its ability to predict flow separation under adverse pressure gradients typical of high-lift wings. Unsteady-RANS (URANS) simulations were also utilized in cases of oscillatory behavior. Simulations were executed on both local hardware and the university's high-performance computing Zaratan cluster.

The final TR25 aerodynamics package was achieved through over 280 design iterations, building upon the baseline of the previous vehicle (TR24). The geometric configuration of the vehicle, illustrated in Fig. 3, features a multi-element front wing, pitot-static tube, 10 pressure taps, nose wing, vortex generators, turning vanes, vortex-driven undertray, biplane rear wing, and full sidepods.

General development simulations consisted of half-car straight-line, constant velocity (56 km/h) simulations. This velocity corresponds to a chord-based Reynolds number of $Re \approx 5\times10^5$, placing the vehicle in a transitional flow regime where boundary layer separation is critical. Comparisons of full-car vs. half-car simulations revealed a difference of less than 1% in force coefficients, confirming that the flow field is largely symmetric in straight-line conditions.

The total volume mesh count for the half-car simulations was approximately 22 million cells. As shown in Fig. 4, a polyhedral mesh with prism layers was utilized to resolve the boundary layer. 8 Prism layers were used, with a near-wall thickness of 0.024 mm, and an absolute size of 8 mm. The mesh was custom-refined to provide accuracy in critical flow regions, specifically the wing element leading and trailing edges, vortex generation zones, and tire wake interactions. Cell size in these refinement regions ranged from 3 mm to 12 mm. To optimize these parameters, a mesh independence study was run, with total cell counts ranging from 10 million to 124 million. The selected 22 million cell design had a 4-times reduction in iteration time, with both downforce and drag values within 1% error of the maximum-refinement solution. All simulations included a moving ground and rotating tires. Each mesh refinement solution during the study

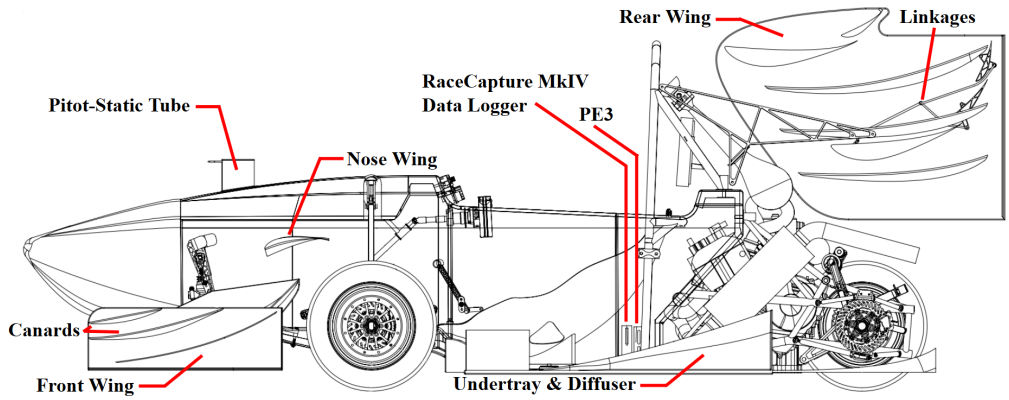
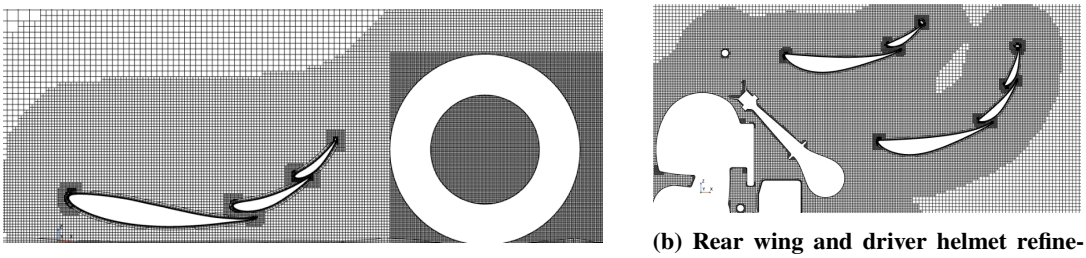


Fig. 3 TR25's side-view engineering drawing.

was compared against the real-world quantitative and qualitative data as outlined at the end of this section.



(a) Front wing and front wheel wake refinement.

(b) Rear wing and driver helmet refinement.

Fig. 4 Longitudinal cross-sectional views of the polyhedral volume mesh showing prism layer inflation and wake refinement zones around the airfoil elements.

In addition to the general development simulations, suites of full-car cornering simulations were run (including varying corner radii, velocities, pitch, roll, yaw, and tire rotation direction), along with ride height sweeps to simulate spring compression under aerodynamic loads.

Figure 5 depicts just a few examples of the hundreds of different CFD analysis tools that went into the design process. Each of these figures is a side-by-side comparison of the (left) high-downforce and (right) low-drag modes.

Figure 5 (a,b) compares the cross-sectional flow fields. In low-drag mode (b), the flow is horizontally oriented (Region 1), with reduced separation behind the nosewing (Region 2) and above the sidepod (Region 3). This reduction in separation increases total pressure at the radiator inlet, correlating to the improved cooling performance.

Figure 5 (c,d) shows an isometric view of the rear-wing wake. These images show the total velocity magnitude of the flow. The high-downforce configuration (c) shows substantial upwash, turbulence, and vorticity in the flow field due to the high-downforce, high-drag nature of the closed mode. The open mode, seen in (d), has a substantial reduction in wake size, turbulence, and vorticity.

Qualitative analysis like this was critical through design iteration cycles, and partnered with quantitative analysis, led to the results of the CFD design discussed next.

B. CFD Design Results

The axis of rotation for each airfoil was selected to be behind the airfoil's center of pressure. This ensures that, in the event of a mechanical failure of the linkage system, the airfoil will fall automatically to its high-downforce configuration due to the aerodynamic moment. Key metrics of the full-vehicle aerodynamic performance for TR25 in both its high-downforce and low-drag configurations are summarized in Table 1.

Ultimately, the TR25 aerodynamic package (compared with TR24) achieved a 7% increase in downforce, a 25.2% reduction in package mass, and a 17% increase in radiator mass flow, resolving systemic cooling problems present in the TR24 platform. The active aerodynamics system (in low-drag mode) further decreased drag by 49% and increased

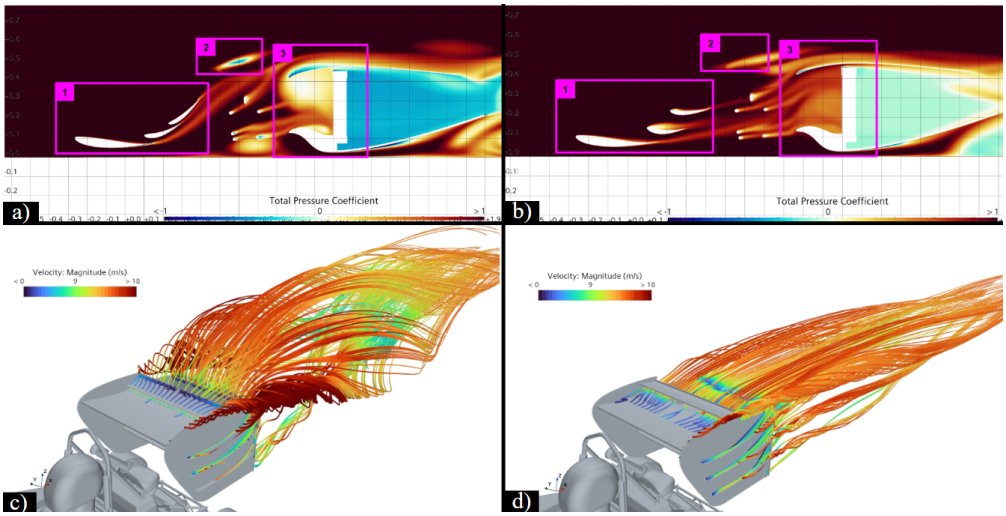


Fig. 5 CFD visualization comparison. (a,b) Longitudinal split-section views of Total Pressure Coefficient around the front-wing and sidepod. (c,d) Isometric views of rear-wing wake Velocity Magnitude. The Left column (a,c) depicts High-Downforce (wings closed), and the Right column (b,d) depicts Low-Drag (wings open).

Table 1 Comparison of TR25 Aerodynamic Performance in Active Modes

Parameter	**High Downforce Mode**	**Low Drag Mode**
Aerodynamic Coefficients		
Downforce Coefficient (C_L)	4.19	1.54
Drag Coefficient (C_D)	1.44	0.73
Lift-to-Drag Ratio (L/D)	2.89	2.10
Forces @ 80 km/h		
Downforce (F_L)	1523 N	560 N
Drag (F_D)	527 N	267 N
Balance & Stability		
Center of Pressure (Front Axle)	48%	40%
Vehicle Constants		
Reference Area (A)	1.24 m^2	
Total Vehicle Mass	215.2 kg	
Center of Mass (Front Axle)	50%	
Aero Package Mass	14.5 kg (7% of total)	

radiator mass flow by an additional 8%, adding only 0.9 kg for the supporting servos, linkages, and electronics.

This increase in mass for the active aerodynamics system was justified through dynamic event simulations in MATLAB. Simulation scripts were created to model the car's full spring/damper dynamics, tire characteristics, cornering behavior, engine power/torque curves, and gearshifts.

The results of these simulations, summarized in Table 2, indicate that the aerodynamic performance gains significantly outweigh the mass penalty. By comparing the active system against a static baseline using 2024 FSAE competition data, the system yields a projected total dynamic event score increase of 34 points (a 10-place overall position gain).

Notably, the center of pressure for the high-downforce mode (48%) has a 2% static margin behind the vehicle's center of mass. This ensures that for varying driver weight distributions (which for the 4 different drivers results in a total center of mass varying from 48.7% to 50.7%), the car always tends towards understeer at high speeds, which is necessary for safety to prevent snap-oversteer. Furthermore, in the low-downforce mode, where the total downforce

Table 2 Projected Performance and Scoring Gains (Active vs. Static Aero)

Event	Performance Delta	Rank Change	Points Gain
Acceleration	−0.08 s	+4	+4
Autocross	−1.47 s	+11	+8
Endurance	−42.0 s	+2	+16
Efficiency	+7.24%	+5	+6
Total	**–**	**+10**	**+34**

is significantly less, increasing the likelihood of losing grip, the center of pressure static margin is increased to 10%, providing rear stability, helping drivers gain confidence when applying throttle for a straight-line portion of a course.

C. CFD Design Validation

To validate the CFD simulation setups, pitot-static tube data, pressure tap data, flow visualization, tufting, constant-radius dynamic, and coast-down dynamic tests were all used. For the scope of this paper, the pressure tap data, tufting, and coast-down dynamic tests will be mentioned.

1. Pressure Taps

For the 10 pressure taps, a Chell nanoDAQ-LTS-16 channel pressure scanner was used (0.3% measurement uncertainty). Tap 8 (light blue) was located in the lower separation region of the radiator (as seen in Fig. 5a), and consistently shows lower pressure, validating the separation pocket seen in CFD. Taps 9 and 10 were located after the radiator, and are consistently lower in pressure than Taps 1-7, which is expected given the radiator's porosity and impact on the flow pressure. Finally, there are large increases in pressure after the system enters low-drag mode (the binary dotted line in its high position), validating the flowfield seen in Fig. 5b), where the low-pressure region in front of the radiator is replaced by the higher-pressure coefficient, darker red, flow. This increase in pressure critically correlates to the 8% increased mass flow while in low-drag configuration, improving engine cooling.

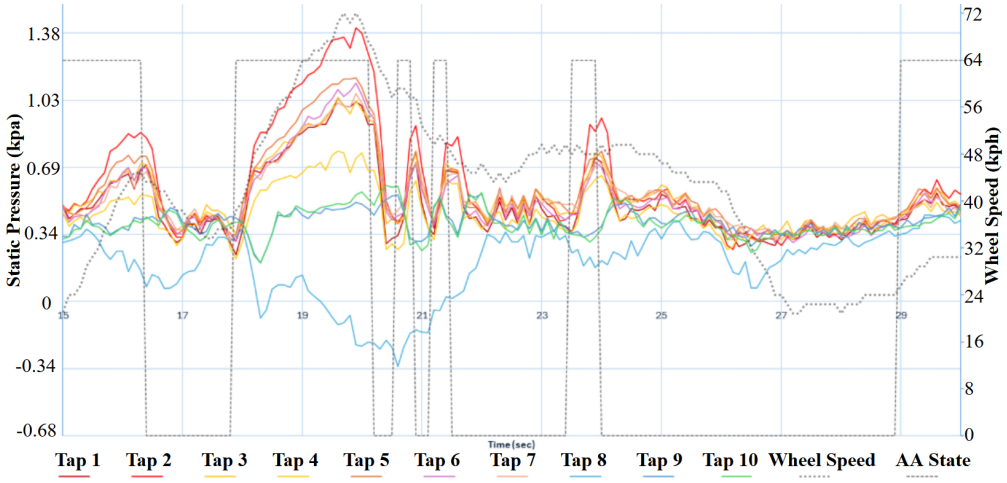


Fig. 6 Sidepod pressure tap data from an Autocross run, with 10 functional pressure taps, dotted line for vehicle speed, and binary dotted line for active aero (AA) system (high is low-drag mode, low is high-downforce mode)

2. Tufting

Figure 7 shows a side-by-side comparison of camera footage during a tufting test of the front wing airfoils (a,b) with high-downforce mode cornering (left) and low-drag mode (right). Comparison with the respective CFD images (c,d) reveals a separation region on the inner side of the upper-most airfoil, validating the CFD setup qualitatively. This

separation region is undesired, ultimately, and is an opportunity for future improvement with the front wing design.

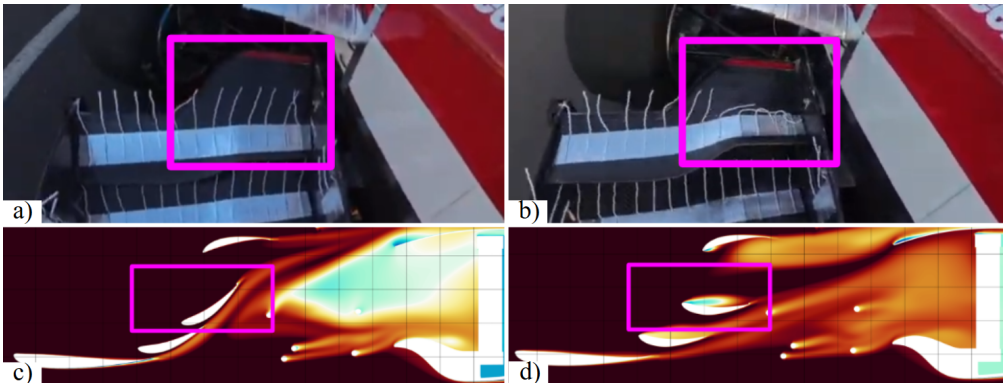


Fig. 7 Validation comparison showing (a,b) camera views of tufting during autocross testing and (c,d) longitudinal split-section CFD views of Total Pressure Coefficient. The Left column depicts High-Downforce (closed) configuration, and the Right column depicts Low-Drag (open) configuration.

3. Coast-down Test

The coast-down test involved using a pull-scale to measure the vehicle's rolling resistance, then, with the vehicle at speed, all engine power was cut, and wheel-speed sensors were used to calculate the drag force on the vehicle. Over multiple trials, the average results showed <1% error in the quantitative drag values found in CFD.

Once the design from CFD was selected, the mechanical implementation was key, and will be discussed next.

D. Mechanical Design

Servos were selected over pneumatic or linear actuators to enable continuous control with minimal mass and complexity. whereas pneumatics are fast, they introduce weight and are inherently binary. Linear actuators were deemed unnecessary as the maximum calculated linkage load was only 133 N. High-torque, waterproof servos (Savox SW-2290SG) were selected for their superior response time and ease of integration. To minimize aerodynamic disturbance, the servos were packaged internally within the main elements of the front and rear wings.

1. Front Wing Development

Three primary iterations of the front wing mechanism were developed and validated using additive manufacturing.

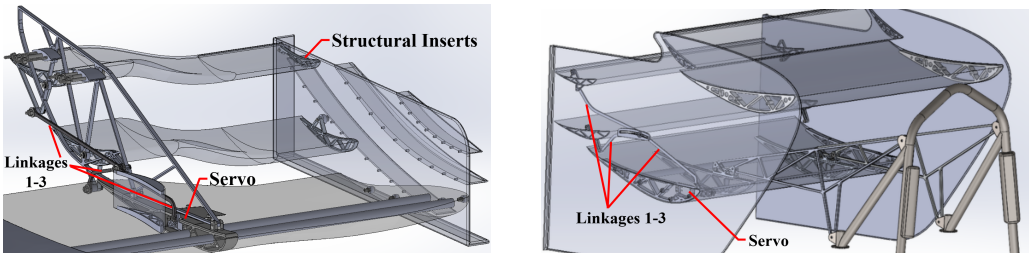
The final structural design (Fig. 8a) utilized linkages waterjet-cut from 3.175 mm 7075-T6 aluminum and a 6.35 mm mounting endplate. Rotating joints employed low-profile steel shoulder bolts and oil-embedded sleeve bearings for reduced friction. The airfoils were manufactured using 3D-printed male molds with a 2-ply carbon fiber wet layup, vacuum bagged for resin distribution. The internal structure featured 3D-printed carbon-fiber-inlayed Onyx inserts to house the servos, accessible via a maintenance panel.

Structural integrity was verified through Finite Element Analysis (FEA) and hand calculations. The design was validated against maximum aerodynamic loads calculated at 112 km/h—the practical top speed for FSAE competitions—as well as a potential head-on cone strike force of 670 N (in FSAE, cones are used to mark the course, and are frequently impacted). The kinematic mechanism employs a slotted endplate to effectively convert the servo's rotary output into linear motion, simplifying the linkage design and packaging. Whereas this architecture proved robust for TR25, it introduces inherent friction; consequently, the next-generation TR26 system currently in development eliminates the slot. Despite the mechanical overhead of the slot, torque calculations at limit velocity yielded a minimum safety factor of 7.02 against servo stall. Finally, two carbon fiber spars span the length of the main element, providing rigidity without the weight penalty of a full foam core.

2. Rear Wing Development

The rear wing utilized a similar three-linkage design. As shown in Fig. 8b, the servo was embedded within the main element, actuating the flaps via 7075-T6 aluminum linkages. The endplates were constructed from spread-tow

carbon fiber with a 3.175 mm Nomex core to increase stiffness-to-weight ratio. Due to higher aerodynamic loads and the larger lever arm required by the rear geometry, the servo safety factor for stall torque was 1.8. Whereas mechanical return springs were considered to ensure fail-safe closure, they were ultimately rejected to avoid further reducing this torque margin. Instead, the system relies on aerodynamic forces for fail-safe operation; analysis confirmed that the maximum servo load occurs at 30% closure, meaning the center of pressure on the elements shifts forward during opening, generating a natural restoring moment that forces the wing closed in the event of actuator failure.



(a) Front Wing assembly (exploded view). **(b) Rear Wing assembly (section view).**

Fig. 8 Final structural design of the active aerodynamic assemblies.

The total mass of the front and rear wing assemblies was 4.99 kg and 5.44 kg, respectively. Despite the addition of servos, linkages, and wiring, the TR25 Rear Wing assembly achieved a 25% mass reduction compared to the TR24 static equivalent. This efficiency was largely driven by the lightweight mechanical design; the aluminum linkages themselves weighed only 80 g for the front wing and 69 g for the rear wing, with fasteners and structural reinforcements adding just 120 g and 80 g, respectively. Consequently, the majority of the active system's mass penalty was concentrated in the servos and electronics rather than the actuation mechanism itself. Whereas the Front Wing saw a slight mass increase of 7.5% due to the two-servo configuration, the rigorous lightweighting of the internal structures and the undertray resulted in a net package weight reduction of 4.58 kg (23.6%). This validates that the implementation of active aerodynamics did not compromise the vehicle's power-to-weight ratio. Design for Manufacturability was prioritized, enabling early completion of the mechanical systems and allowing ample testing time for the electronics and control algorithms.

IV. Electronics and Controls Design

The active aerodynamics system relies on a robust electronics architecture designed to process high-frequency sensor data and execute precise actuation commands in the harsh vibration and thermal environment of a race car. The system is divided into three primary layers: sensor data acquisition, central processing, and actuation.

A. Hardware Architecture

The core of the control system was a custom electronics enclosure housing an Adafruit Feather RP2040 CAN microcontroller. This unit, the central processing node, interfaced with the vehicle's CAN bus to receive telemetry from the RaceCapture data logger. The system integrated data from seven vehicle sensors and three driver inputs:

- **Vehicle Sensors:** Steering Angle, Throttle Position (TPS), Y-Acceleration, X-Acceleration, Brake Pressure, Wheel Speed (Front Left), Wheel Speed (Front Right).
- **Driver Inputs:** Low DF Switch (Overrides the system to low-drag mode for the Acceleration event only), Active Aero Switch (Turns the autonomous control on/off), Sensitivity Knob (adjustment for the sensitivity of the FSM state transitions, which can be tuned for each driver, and varying track conditions).

Power distribution is managed via a dedicated 12V rail from the vehicle's main harness, which is stepped down to 8.4V for the servos and 5V for the logic circuits. To ensure reliability, each servo channel is isolated with individual 5A fuses, preventing a single actuator failure from compromising the entire system.

B. Finite State Machine (FSM) Logic

To manage the complex decision-making required for autonomous operation, a Finite State Machine (FSM) was implemented on the RP2040 microcontroller. Unlike simple threshold-based logic, the FSM incorporates hysteresis and fault tolerance to ensure stability in the noisy data environment of a race car. The choice to use an FSM meant that the

system would be simple and easy to tune, which was required for a fast turnaround and reliability. The hardware has potential for much more complex methods of control in future implementation.

C. State Definitions and Hysteresis

Whereas the mechanical system supports continuous actuation, the control logic utilizes two primary physical states to maximize predictability for the driver:

1) **High Downforce (State 0):** The default safety state. Wings are set to maximum angle of attack to maximize lateral grip (F_y) and aerodynamic drag (F_D) for braking.
2) **Low Drag (State 2):** The wings are set to their open position to minimize drag during straight-line acceleration.

Early testing revealed that binary switching could cause actuator chatter when vehicle dynamics hovered near threshold values. To mitigate this, the FSM includes a logical buffer (internal State 1). In this intermediate zone, the system holds the *previous* physical state until a distinct exit threshold is crossed. For example, while the system enters Low Drag at $< 0.5g$ lateral acceleration, it will not revert to High Downforce until lateral acceleration exceeds $1.1g$ (or another trigger occurs), preventing oscillation during minor steering corrections on straights.

D. Transition Logic

Transitions are governed by Boolean logic equations derived from vehicle dynamics thresholds, where the symbol $\wedge$ denotes the logical AND operator, $\vee$ denotes the logical OR operator, and $\neg$ denotes the logical NOT operator. The system utilizes a three-state logic model (High Downforce, Medium/Buffer, Low Drag) to manage hysteresis.

To accommodate varying driver styles, the throttle activation threshold, T_{thresh}, is not a static constant. Instead, it is dynamically adjusted by the driver via a dashboard potentiometer, the "Sensitivity Knob." This allows the activation threshold to vary between 10% and 30% throttle, enabling the driver to bias the system towards aggressive drag reduction or conservative stability based on track conditions.

The transition from *High Downforce* (State 0) to *Low Drag* (State 2) is triggered only when the vehicle is confirmed to be in a stable straight-line acceleration event. This conservative logic ensures that the system never reduces downforce if the driver is modulating the throttle or steering (evidence of the vehicle being grip-limited rather than power-limited).

The complete state transition logic is defined by Eqs. (2) through (7):

$$\text{Transition}_{0\to2} = ((T > T_{thresh}) \vee ((T > 80) \wedge (V > 24))) \wedge (\delta < 30) \wedge (|a_y| < 0.5) \wedge (P_{brake} < 30) \tag{2}$$

$$\text{Transition}_{0\to1} = \neg(\text{Transition}_{0\to2}) \wedge (V > 24) \wedge (|a_y| < 1.1) \wedge (\delta < 30) \wedge (P_{brake} < 50) \wedge (a_x < 0.4) \tag{3}$$

$$\text{Transition}_{1\to0} = (P_{brake} > 30) \vee (a_x > 0.3) \vee (\delta > 40) \vee (|a_y| > 1.1) \tag{4}$$

$$\text{Transition}_{1\to2} = \neg(\text{Transition}_{1\to0}) \wedge (|a_y| < 0.5) \wedge (\delta < 20) \wedge (T > T_{thresh}) \tag{5}$$

$$\text{Transition}_{2\to0} = (T < T_{thresh}) \wedge \big((\delta > 40) \vee (|a_y| > 1.1) \vee (P_{brake} > 30) \vee (a_x > 0.3)\big) \tag{6}$$

$$\text{Transition}_{2\to1} = \neg(\text{Transition}_{2\to0}) \wedge (V > 24) \wedge \big((|a_y| > 0.5) \vee (\delta > 20)\big) \tag{7}$$

where T is throttle position (%), V is vehicle speed (km/h), δ is steering angle (deg), a_y is lateral acceleration (g), a_x is longitudinal acceleration (g), and P_{brake} is brake pressure (psi).

E. Signal Conditioning and Fault Tolerance

To handle the potential for sensor failures, the software implements a graceful degradation strategy. Raw sensor data are filtered to remove noise. If a sensor dropout is detected, the algorithm applies a zero-order hold, retaining the last valid data point for one cycle. If the fault persists, the FSM automatically defaults to the High Downforce state. This ensures that a sensor failure (e.g., loss of steering angle data) results in a safe, high-grip configuration rather than an unpredictable low-drag state entering a corner. Additionally, the sensor suite was selected such that every vehicle state is corroborated by two independent inputs (e.g., lateral acceleration a_y correlating with steering angle δ, or brake pressure P_{brake} correlating with longitudinal acceleration a_x).

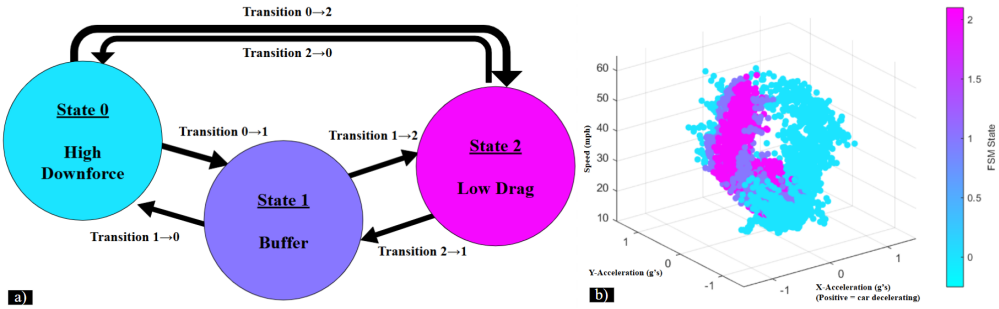


Fig. 9 (a) State transition logic governing the switch between High Downforce and Low Drag. (b) 3D scatter plot of recorded telemetry data colored by FSM state. Clear clustering indicates robust state separation.

F. Actuator Protection Strategy

To mitigate the risk of servo overheating under sustained aerodynamic loads, and to reduce system noise and power consumption, a detach logic was implemented. The firmware monitors the time elapsed since the last state change command. If the system remains in a static state for more than 500 ms, the Pulse Width Modulation (PWM) signal to the servos is disabled. This relies on the mechanical advantage of the linkage system and the internal friction of the servo geartrain to hold the wing position, significantly reducing average power consumption and thermal stress on the actuators. Given that the servos have a self-centering mode that consumes significant power trying to correct for negligible misalignments in the linkages in certain positions, this addition is particularly beneficial while waiting in line for an autocross run or when the car is warming up.

V. Track Testing Results

Track testing was conducted to validate the autonomous decision-making capabilities of the active aerodynamics system. Telemetry data were logged at 50 Hz using the onboard RaceCapture system during dynamic testing sessions. The primary objectives of the analysis were to verify the stability of the FSM and to confirm that the Low Drag state was activated exclusively during safe, straight-line acceleration events.

A. Logic Validation and State Space Analysis

The robustness of the control logic is visualized in Fig. 9. This 3D scatter plot maps the vehicle's operating points across three dimensions: Longitudinal Acceleration (X), Lateral Acceleration (Y), and Speed.

The data reveal a distinct separation of states, forming a donut topology. The High Downforce state (Cyan) dominates the high-lateral-acceleration regions (cornering) and positive longitudinal-acceleration regions (braking). The Low Drag state (Magenta) forms a clustered band exclusively in the high-speed, low-lateral-G region. Crucially, there is minimal noise at the boundaries, confirming that the hysteresis buffers successfully prevented rapid oscillation between states during transient maneuvers.

B. Spatial and Dynamic Performance

To verify the system's behavior in a race environment, FSM state data were analyzed spatially and temporally, as shown in Fig. 10. The Global Positioning System (GPS) overlay (a) demonstrates spatial awareness without requiring GPS inputs. The Low Drag state (Magenta) activates early in straights as the driver applies throttle and reduces steering angle. Conversely, the system reverts to High Downforce (Cyan) upon braking or turn-in. Note the consistency in the braking zones at the end of long straights; the system reliably restores maximum downforce *before* the vehicle enters the high-lateral-G cornering phase. This validates the override logic defined in Eq. (6) while maximizing braking potential.

A valuable test case is observed in the large sweeping corner (bottom right of the track map). Here, the vehicle transitions between grip-limited and power-limited states depending on the driver's style. The FSM successfully maintained High Downforce when the car was grip-limited and switched to Low Drag when power-limited, confirming the system's robustness even in ambiguous cornering scenarios.

The time-series telemetry (b) confirms the temporal response, showing successful actuation cycles. The correlation between vehicle speed and state activation is evident, with the system consistently engaging Low Drag as speed increases

on straights and disengaging as speed drops during braking events.

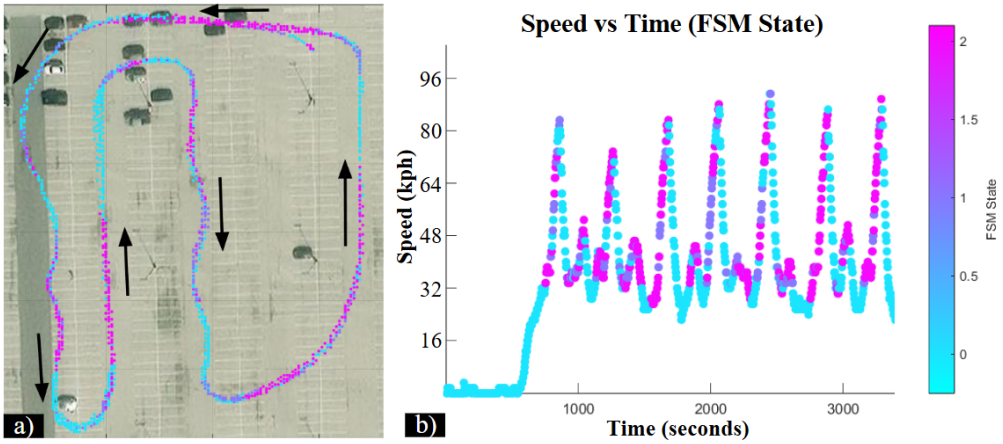


Fig. 10 Combined telemetry analysis showing (a) GPS track map overlay and (b) time-series speed data colored by FSM state, showing successful state transitions during track testing on an autocross course.

VI. Conclusion

The autonomous active aerodynamics system presented in this work was successfully deployed on the Terps Racing TR25 vehicle during the 2025 Formula SAE Internal Combustion competition at Michigan International Speedway. The system demonstrated robust operation throughout all dynamic events, culminating in the successful completion of the 22 km Endurance race without mechanical or software failure. This reliability, combined with the demonstrated performance benefits, resulted in the system receiving a Second Place Innovation Award.

Whereas the current implementation successfully solved the drag-versus-downforce conflict, the architecture provides a foundation for more advanced vehicle dynamics control. Future development for the TR26 vehicle will focus on transitioning from discrete state switching to continuous, variable actuation. By actively modulating the longitudinal C_p in real-time, the aerodynamic package can be coupled with the suspension system to actively correct for understeer and oversteer transients, effectively using the wings as control surfaces for yaw stability.

Additionally, future mechanical iterations will prioritize weight optimization and increased actuation redundancy to further improve the system's safety factor. Finally, the integration of higher-fidelity telemetry will enable the development of data-driven control models, such as neural networks, to predict optimal aerodynamic configurations based on predictive track mapping rather than reactive sensor thresholds.

Acknowledgments

The authors thank the University of Maryland Terps Racing team for their support and resources. Significant technical contributions were provided by Eamon Goff (electronics and control logic), Steven Ying (mechanical design), J. M. Gallo (CFD analysis), and Sam Kashima (manufacturing). The authors also gratefully acknowledge the testing and driver teams for their essential role in system validation and tuning.

References

[1] Milliken, W. F., and Milliken, D. L., *Race Car Vehicle Dynamics*, SAE International, Warrendale, PA, 1995.

[2] Katz, J., *Race Car Aerodynamics: Designing for Speed*, 1st ed., Bentley Publishers, Cambridge, MA, 1995.

[3] SAE International, *Formula SAE Rules 2025*, Society of Automotive Engineers, Warrendale, PA, 2024. Version 1.0.

[4] Merkel, J. P., "Development of Multi-Element Active Aerodynamics for the Formula SAE Car," Master's thesis, The University of Texas at Arlington, Arlington, TX, May 2014.